RSC Applied Polymers

ROYAL SOCIETY OF CHEMISTRY

PAPER

View Article Online
View Journal | View Issue

Check for updates

Cite this: *RSC Appl. Polym.*, 2025, **3**, 146

Nanostructuring niobium oxides using polymer-grafted cellulose nanocrystals and nanofibers as sacrificial scaffolds†

Yen Theng Cheng,[a,b] Sandya S. Athukoralalage,[c] Nasim Amiralian,[c] Chris D. Ling[b,d] and Markus Müllner*[a,b]

Received 7th June 2024,
Accepted 27th August 2024

DOI: 10.1039/d4lp00185k

rsc.li/rscapplpolym

The unique one-dimensional structure and surface functionality of cellulose nanocrystals (CNCs) and cellulose nanofibers (CNFs) render them promising candidates for renewable nanomaterials. Here, we report the template-directed synthesis of highly polycrystalline Nb_2O_5 polymorphs using polymer brush-grafted CNCs and CNFs as sacrificial scaffolds. The scaffolds consisted of a CNC or CNF core, from which poly(2-(dimethylamino)ethyl methacrylate) (PDMAEMA) brushes were grafted using surface-initiated atom transfer radical polymerization (SI-ATRP). The nanocellulose-*g*-PDMAEMA nanoreactors were complexed with a water-soluble Nb_2O_5 precursor, ammonium niobate(v) oxalate hydrate (NbO*x*A), *via* electrostatic interaction before they were heated to different temperatures to fabricate one-dimensional polycrystalline niobium pentoxides (*nc*-Nb_2O_5 and *nf*-Nb_2O_5) with controllable polymorphism. Specifically, phase-pure pseudohexagonal Nb_2O_5 (TT-Nb_2O_5), orthorhombic Nb_2O_5 (T-Nb_2O_5) and monoclinic Nb_2O_5 (H-Nb_2O_5) were synthesized. Finally, we show that the polycrystalline *nc*-Nb_2O_5 and *nf*-Nb_2O_5 can function as photocatalysts for decomposing rhodamine B.

Introduction

Biopolymers hold great potential as key components in fabricating advanced hybrid materials owing to their sustainability and ubiquitous availability. Within this framework, nanocelluloses, a general term used for cellulose nanocrystals (CNCs) and cellulose nanofibers (CNFs), stand out as leading candidates due to their exceptional mechanical properties, distinctive physical properties, high crystalline order and chirality, along with their remarkable attributes such as cost-effectiveness and ease of processing into larger-scale materials. In addition, CNCs and CNFs enable the design of nanomaterials where high aspect ratio and interconnectedness play important roles.[1–6] They have a multitude of applications, including strengthening the mechanical properties of polymer films[7,8] and developing advanced functional materials such as viscosity modifiers,[9] stabilizers for Pickering emulsions,[10–12] heterogeneous catalyst supports,[13] antibacterial agents[14] and antifouling/separation membranes.[15,16]

The intrinsic high aspect ratios of CNCs and CNFs, with lateral dimensions at the nanoscale, spanning from nanometers to micrometers in length, along with tunable surface functionalities render them well suited for preparing 1D anisotropic hybrid nanomaterials. Specifically, nanocellulose surface modification with polymer brushes has proved to be a robust approach for preparing 1D core–shell particles that can function as nanoreactors to fabricate energy-storing, optoelectronic and catalytic nanomaterials.[17–19]

Nanostructured metal oxides have been extensively researched as they hold great promises for a plethora of applications including, but not limited to, catalysis, sensing and energy storage.[17,20,21] Among these, niobium pentoxide (Nb_2O_5) has garnered great attention due to its non-toxic nature and strong redox ability.[22–24] Nb_2O_5 can be synthesized in several structural forms, including amorphous and crystalline pseudohexagonal phases (TT-Nb_2O_5), an orthorhombic phase (T-Nb_2O_5), and a monoclinic phase (H-Nb_2O_5), depending on factors such as temperature and processing time. This polymorphism underlies the versatility of Nb_2O_5 for

[a]*Key Centre for Polymers and Colloids, School of Chemistry, The University of Sydney, Sydney, NSW 2006, Australia. E-mail: markus.muellner@sydney.edu.au*
[b]*The University of Sydney Nano Institute (Sydney Nano), Sydney, NSW 2006, Australia*
[c]*Australian Institute of Bioengineering and Nanotechnology (AIBN), The University of Queensland, 4072 St Lucia, Queensland, Australia*
[d]*School of Chemistry, The University of Sydney, Sydney, NSW 2006, Australia*

† Electronic supplementary information (ESI) available: Materials, methods, and supplementary results, including polymer and hybrid characterization, electron microscopy, physisorption and electrochemical performance studies. See DOI: https://doi.org/10.1039/d4lp00185k

applications, particularly as photocatalysts[23,25,26] and energy-storing materials.[27] While various morphologies have been reported for Nb_2O_5, such as nanobelts,[28] nanosheets[29,30] and nanowires,[31] the nanostructuring of Nb_2O_5 remains largely unexplored.

In this work, a series of one-dimensional, polycrystalline Nb_2O_5 samples with different crystalline phases were synthesized using soft-templating polymer-grafted nanocelluloses (Scheme 1). CNC-*g*-PDMAEMA and CNF-*g*-PDMAEMA were prepared through surface-initiated atom transfer radical polymerisation (SI-ATRP) of DMAEMA from their corresponding nanocellulose-based polyinitiator, CNC-Br or CNF-Br. A water-soluble niobium salt, ammonium niobate(v) oxalate dihydrate (NbO*x*A), was loaded into the polyelectrolyte PDMAEMA shell of CNC-*g*-PDMAEMA and CNF-*g*-PDMAEMA. By calcining the NbO*x*A-loaded nanocellulose polymer brushes at different temperatures, phase-pure pseudohexagonal, orthorhombic, and monoclinic Nb_2O_5 samples were fabricated. Subsequently, the photocatalytic activities of the various nanostructured oxides were tested.

Experimental section

Preparation of pristine CNFs

Purified sugarcane trash pulp was first produced using the method reported before.[10] Washed and ground fibres were treated with a 2% (w/v) sodium hydroxide solution using a 10 : 1 solvent to trash ratio at 80 °C for two hours, followed by rinsing with 60 °C water. The alkali-treated fibres were then bleached twice using an acidic solution of 1% (w/v) sodium chlorite (pH = 4, the pH was decreased using glacial acetic acid) at 70 °C for one hour at a 30 : 1 solvent to fibre ratio. Cellulose nanofibers (CNFs) were prepared by passing a 0.7% (w/v) dispersion of bleached pulp through a high-pressure homogenizer (GEA Niro-Soavi Panda NS1001 L 2 K Homogenizer), for one pass at 400 bar, one pass at 800 bar and three passes at 1100 bar. For the production of H_2SO_4-treated fibres, the bleached pulp was treated with a 40% (v/v) H_2SO_4 solution at 45 °C for 3 hours. After hydrolysis, the fibre dispersion was centrifuged for 15 minutes at 10 000 rpm 4 times to remove the excess acid and dissolved extractables.

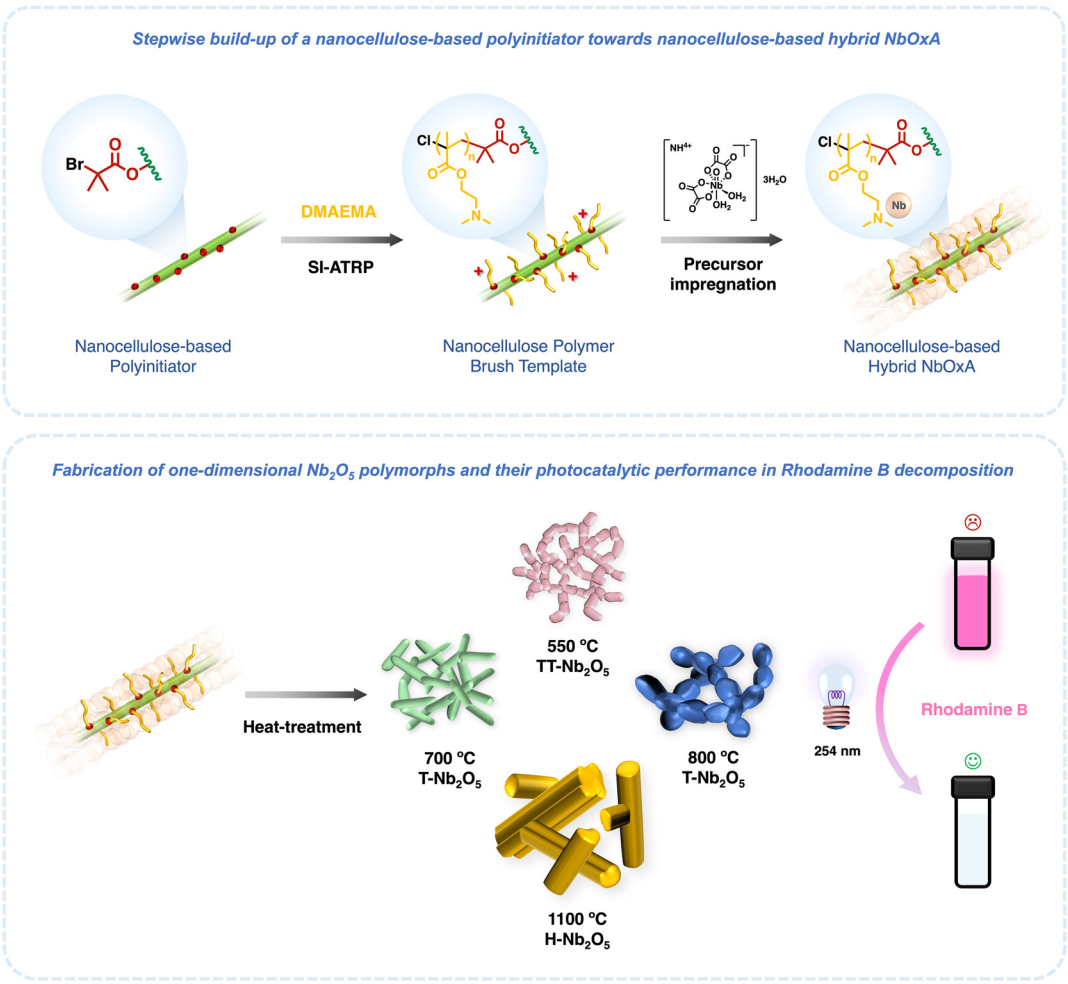

Scheme 1 Template-directed fabrication of Nb_2O_5 polymorphs using nanocellulose-based polymer brush templates.

Subsequently, the resulting precipitate was dialysed in deionised water for one week until a pH value of 7 was achieved, and then re-suspended in deionised water using an ultrasonic probe (Q500 Sonicator, QSonica Newtown, United States) set at 25% amplitude, with a frequency of 20 kHz and an output energy of 500 W for 5 minutes.

Preparation of CNC-Br and CNF-Br polyinitiators

Pristine CNCs or CNFs (0.300 g, 1.85 mmol) were dispersed in DMF (300 mL) to achieve a homogeneous suspension, facilitated by sonication using a Soniclean 120T sonicator (240 V, 50/60 Hz) for 10 min. To the nanocellulose suspension, triethylamine (TEA, 0.562 g, 5.55 mol) and 4-dimethylaminopyridine (DMAP, 22.6 mg, 1.85×10^{-1} mmol) were added. The nanocellulose suspension was later cooled to 0 °C in an ice bath. After stirring for 30 minutes, α-bromoisobutyryl bromide (α-BiBB, 1.28 g, 5.55 mmol) was introduced dropwise into the cold nanocellulose suspension. The esterification reaction was allowed to proceed overnight. The resulting polyinitiator was purified through multiple cycles of centrifugation and redispersion in DMF (3 × 45 mL) and water (1 × 45 mL). The CNC-Br and CNF-Br polyinitiators were freeze-dried from milliQ water. The mass percentage of bromine (Br wt%) was determined using elemental analysis.

Preparation of CNC-*g*-PDMAEMA and CNF-*g*-PDMAEMA nanoreactors

The general procedure for the grafting-from SI-ATRP of the polymer brush-grafted nanocellulose is as follows. The CNC-Br polyinitiator (100 mg, n(Br) = 2.5×10^{-2} mmol), DMAEMA (1.05 mL, 6.2 mmol), PMDETA (13 mg, 7.5×10^{-2} mmol) and DMF (20 mL) were mixed. The reaction mixture was degassed by four freeze–pump–thaw cycles with N_2. Subsequently, CuCl (2.5 mg, 2.5×10^{-2} mmol) was introduced into the frozen reaction mixture under a gentle N_2 flow. The SI-ATRP reaction was initiated at 65 °C after the final freeze–pump–thaw cycle. The polymerisation was terminated after 2 h by exposure to atmospheric air and cooling to room temperature. CNF-*g*-PDMAEMA was synthesized following the same procedure by substituting CNC-Br with CNF-Br. The resulting polymer-grafted nanocellulose was purified by several cycles of centrifugation and redispersion in DMF (3 × 45 mL) and water (1 × 45 mL) before they were freeze-dried from water. Monomer conversions for CNC-*g*-PDMAEMA and CNF-*g*-PDMAEMA were 10% and 8%, respectively, as determined from changes in the characteristic ^{1}H NMR integrals. The degrees of polymerisation (DP) were calculated to be $PDMAEMA_{25}$ and $PDMAEMA_{21}$, respectively, assuming all initiation sites were initiated during polymerisation. The same reaction was conducted using a sacrificial initiator, ethyl α-bromoisobutyrate (EBiB, 8.0 mg, 4.1×10^{-2} mmol), to evaluate the control of polymerisation.

Synthesis of nanostructured Nb_2O_5 using polymer-grafted nanocelluloses

In a typical hybrid synthesis, the polymer-grafted nanocellulose, CNC-*g*-PDMAEMA (0.300 g, 1.45 mmol DMAEMA) or CNF-*g*-PDMAEMA (0.300 g, 0.94 mmol DMAEMA), was dispersed in water to obtain a homogeneous suspension (0.5 mg mL^{-1}) by sonication for 10 min. To facilitate NbO*x*A complexation with the PDMAEMA brush, the pH of the suspension was adjusted to pH 2 using 1.0 M HCl to increase the degree of DMAEMA protonation. The nanocellulose polymer brush suspensions were added dropwise to the NbO*x*A solution (2.2 g, 7.3×10^{-2} mmol/2.1 g, 7.1×10^{-2} mmol, 5 eq.). The infiltration process was allowed to proceed overnight. The as-synthesised *nc*-NbO*x*A and *nf*-NbO*x*A hybrids were purified by several cycles of centrifugation and redispersion in water (3 × 45 mL), in which the free NbO*x*A in the supernatant layer in each cycle was removed after centrifugation. The purified hybrids were subsequently freeze-dried from water before they were calcined in air at different controlled temperatures for either 2 hours (Nb_2O_5-550, Nb_2O_5-700, and Nb_2O_5-800) or 10 hours (Nb_2O_5-1100).

Synthesis of bulk pseudohexagonal Nb_2O_5

The NbO*x*A powder (100 mg, 3.3×10^{-1} mmol) was calcined at 550 °C for 2 hours.

Photocatalytic activity measurements

The photocatalytic activities of the *nc*-Nb_2O_5 and *nf*-Nb_2O_5 samples were assessed by degrading rhodamine B. The photocatalytic reactions were performed in a vial at room temperature. For each run, the Nb_2O_5 photocatalyst (15 mg) was added to the rhodamine B solution (30 mg L^{-1}, 20 mL) in milliQ water. The slurry was then placed in a Rayonet RPR-100 photochemical reactor under illumination with 16 UV-C lamps (maximum intensity at 254 nm). To obtain the adsorption–desorption equilibrium, the samples were stirred continuously in the dark for 15 minutes. Aliquots of the slurry (1.5 mL) were taken every 30 minutes and centrifuged to remove the catalyst prior to spectrometric analysis.

Results and discussion

SI-ATRP as a means to graft polymer chains from surfaces and particles is well established[4,32,33] and has been successfully extended to nanocelluloses.[6,34,35] The synthesis of CNC-*g*-PDMAEMA and CNF-*g*-PDMAEMA is illustrated in Scheme 1. Pristine CNCs and CNFs were prepared following a previously reported protocol (ESI, Fig. S1†).[12] It should be noted that nanocelluloses with a low aspect ratio (<100), typically obtained *via* an acid hydrolysis process, are commonly called "cellulose nanocrystals" (CNCs). In order to avoid confusion, the wood-derived commercial nanocellulose is called CNC and the high aspect ratio sugarcane acid hydrolyzed fibre is called CNF in this study. The hydroxyl groups on the surfaces of pristine CNCs and CNFs were esterified to ATRP initiator sites using α-BiBB, effectively functioning as 1D polyinitiators (CNC-Br and CNF-Br). The successful introduction of ATRP initiators onto the surfaces of pristine CNCs and CNFs was verified using FTIR, where the appearance of new stretching

bands at 1723 cm^{-1} (CNC-Br) and 1716 cm^{-1} (CNF-Br) revealed the presence of carbonyl functionalities of the initiators. Elemental analysis of CNC-Br and CNF-Br elucidated bromine contents of 2% by mass, respectively, corresponding to a degree of substitution of approximately 12% on the nanocellulose surface (Fig. 2a).

Subsequently, PDMAEMA polymer side chains were grafted *via* SI-ATRP using the "grafting-from" approach. Using the sacrificial initiator approach,[36] the controlled character of the polymerisations were demonstrated by linear first-order kinetic plots ($\ln[M_0]/[M]$ against time (ESI, Fig. S2†). The corresponding monomer conversions progressed in a linear fashion from 0 to 4 hours. The resulting sacrificial PDMAEMA-free polymers also showed dispersities ($Đ$) of 1.12 and 1.13 (ESI, Fig. S3†). The ^{1}H NMR spectra of CNC-*g*-PDMAEMA and CNF-*g*-PDMAEMA with peak assignments are shown in Fig. 1b. Qualitative examination *via* FTIR confirmed the presence of PDMAEMA side chains in both nanocellulose-based polymer brushes (Fig. 1a). This confirmation was highlighted by a more prominent C=O stretching band and an additional band at 1440 cm^{-1}, suggestive of carbonyl and *N*-methyl functionalities of the PDMAEMA side chains.

In an acidic aqueous environment, the PDMAEMA side chain-enriched shell enveloping the nanocelluloses is positively charged, thereby orchestrating the complexation of negatively charged niobate precursors to yield their corresponding hybrids, *nc*-NbO*x*A (CNC-*g*-PDMAEMA@NbO*x*A) and *nf*-NbO*x*A (CNF-*g*-PDMAEMA@NbO*x*A). The selection preference for the water-soluble NbO*x*A stems from its superior stability in water relative to its alternative water-insoluble precursor, niobium pentachloride ($NbCl_5$), which undergoes rapid hydrolysis under aqueous conditions, leading to premature decomposition that forms Nb_2O_5.[37] Scanning electron microscopy (SEM) images of *nc*-NbO*x*A and *nf*-NbO*x*A are shown in Fig. S4.† Thermogravimetric analysis (TGA) was used to determine the weight content of Nb_2O_5 in both the *nc*-NbO*x*A and *nf*-NbO*x*A hybrids, indicating substantial incorporation of Nb_2O_5 within the nanocellulose brush templates (Fig. 1c), specifically, 44 wt% for *nc*-NbO*x*A and 42 wt% for *nf*-NbO*x*A. These weight contents are in line with their comparable side chain lengths, highlighting consistency among the samples.

Next, to generate *nc*-Nb_2O_5 and *nf*-Nb_2O_5 and study their crystalline phases as a function of calcination temperature, the *nc*-NbO*x*A and *nf*-NbO*x*A hybrids were subjected to controlled

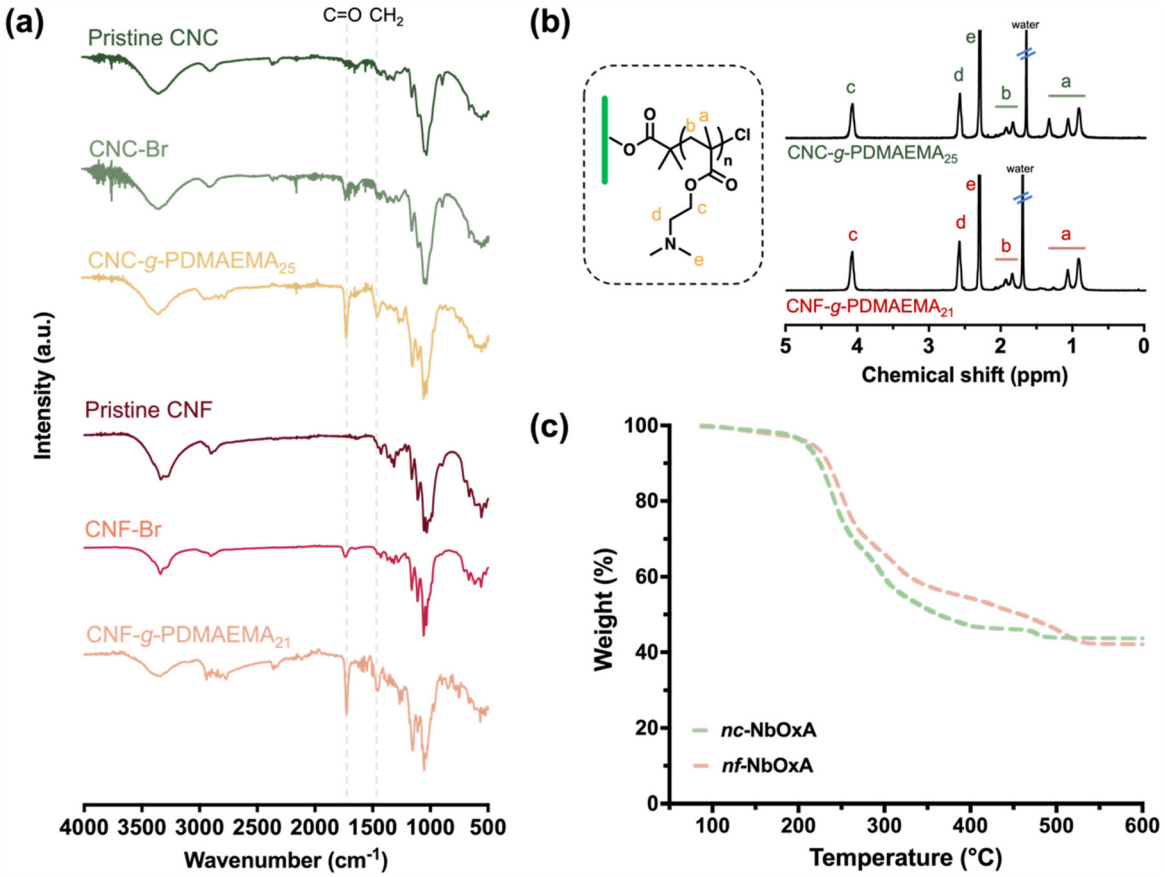

Fig. 1 (a) FTIR spectra of pristine, ATRP initiator-functionalised and PDMAEMA-grafted CNFs and CNFs. The emergence of a carbonyl peak at 1728 cm^{-1} validates the incorporation of ATRP initiators on CNC-Br and CNF-Br. The more pronounced peaks at 1728 cm^{-1} and 1442 cm^{-1} indicate the presence of PDMAEMA polymer side chains. (b) ^{1}H NMR spectral assignments for CNC-*g*-$PDMAEMA_{25}$ and CNF-*g*-$PDMAEMA_{21}$ recorded in $CDCl_3$. (c) TGA profiles of the hybrids of CNC-*g*-$PDMAEMA_{25}$ and CNF-*g*-$PDMAEMA_{21}$ in air.

heating at temperatures of 550 °C, 700 °C, 800 °C and 1100 °C with the dual purpose of removing all organic materials (ESI, Fig. S5†) and inducing crystallisation towards metal oxides. Morphological changes among the samples were observed using SEM and TEM (Fig. 2). In addition, powder X-ray diffraction (PXRD) was employed to evaluate changes in the crystalline phases (Fig. 3), and their average crystallite sizes were estimated using the Scherrer equation.[38]

At 550 °C, both *nc*-Nb_2O_5-550 and *nf*-Nb_2O_5-550 display a phase-pure pseudohexagonal Nb_2O_5 structure (Fig. 3a and b), with an average particle diameter of 20 nm (Fig. 2a and b). Their crystallite sizes were estimated to be 25 nm and 23 nm, respectively, using the Scherrer equation. In the case of *nc*-Nb_2O_5-550, the particles show an arrangement reminiscent of 2D thin sheet-like structures, while in the *nf*-Nb_2O_5-550 sample, the particles appear to be fibre-like, which can be attributed to the fibrous nature inherent in CNFs. Upon adjusting the calcination temperature to 700 °C, a different crystalline phase emerged, as evidenced in Fig. 3b, which shows phase-pure orthorhombic Nb_2O_5 (T-Nb_2O_5) structures. The

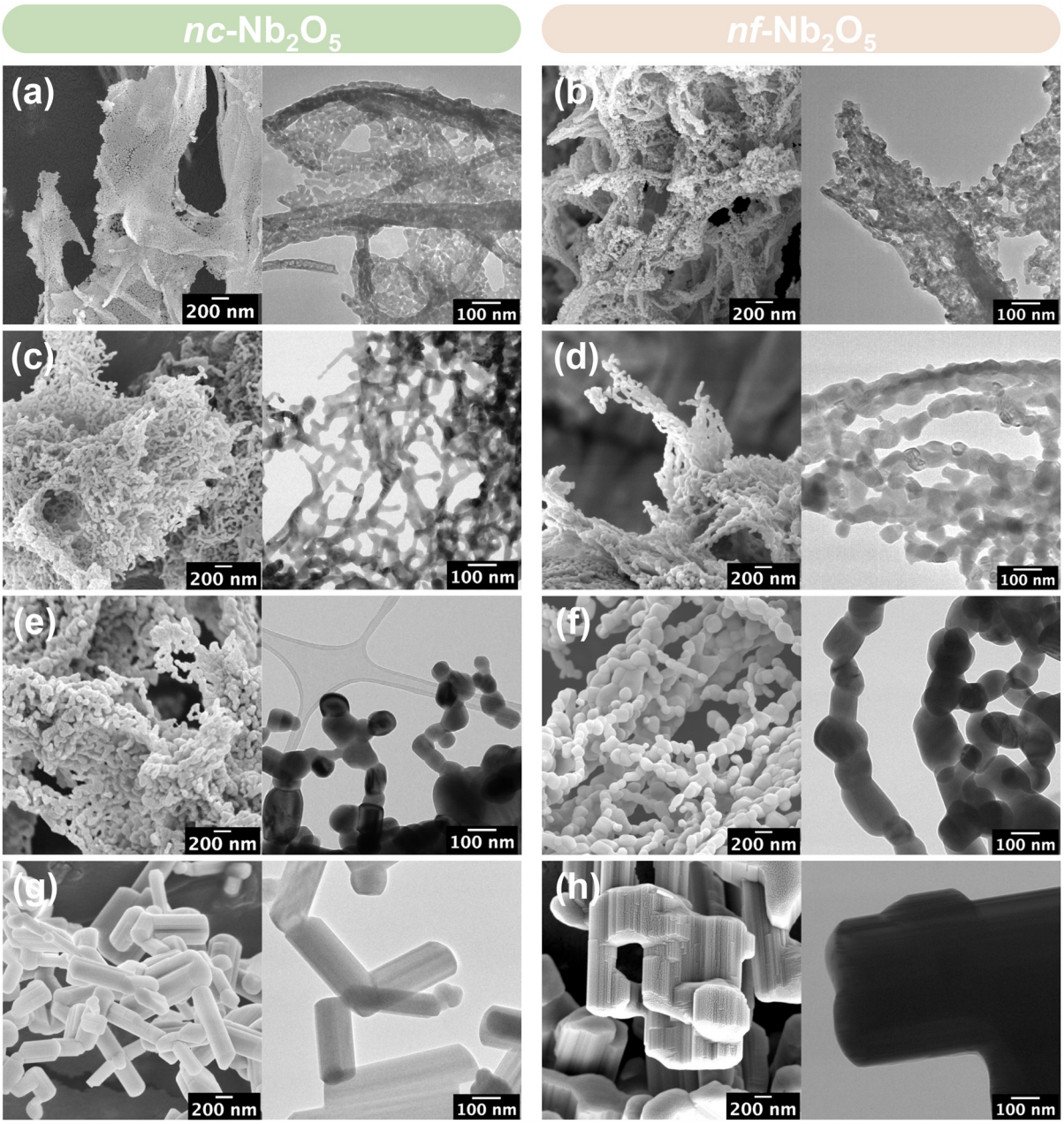

Fig. 2 SEM and TEM micrographs of *nc*-Nb_2O_5 and *nf*-Nb_2O_5 synthesised at (a and b) 550 °C, (c and d) 700 °C, (e and f) 800 °C and (g and h) 1100 °C.

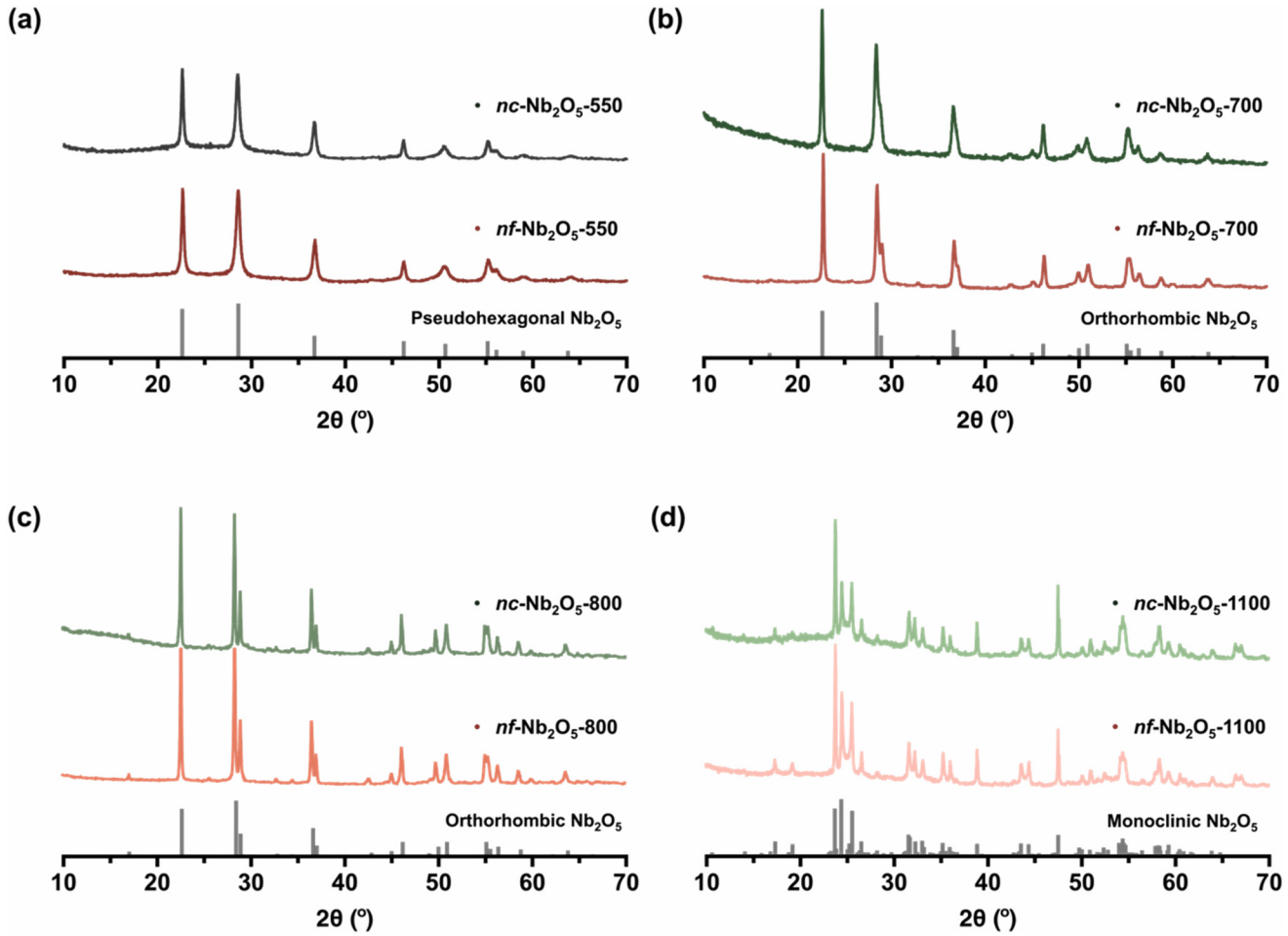

Fig. 3 PXRD data (Cu K_α, λ = 1.5406 Å) for (a) *nc*-Nb_2O_5-550 and *nf*-Nb_2O_5-550, (b) *nc*-Nb_2O_5-700 and *nf*-Nb_2O_5-700, (c) *nc*-Nb_2O_5-800 and *nf*-Nb_2O_5-800 and (d) *nc*-Nb_2O_5-1100 and *nf*-Nb_2O_5-1100. The reference Bragg diffraction peaks of the corresponding Nb_2O_5 crystalline phases are shown at the bottom of each plot.

particles of orthorhombic *nc*-Nb_2O_5-700 and *nf*-Nb_2O_5-700 appear rod-like in shape (Fig. 2c and d). Despite their comparable morphologies, *nf*-Nb_2O_5-700 exhibits a larger average crystallite size of 56 nm compared to *nc*-Nb_2O_5-700 which has an average crystallite size of 34 nm. Increasing the calcination temperature to 800 °C did not lead to a transition in the crystalline phase of the Nb_2O_5 structure (Fig. 3c). However, the PXRD peaks of *nc*-Nb_2O_5-800 and *nf*-Nb_2O_5-800 narrowed due to increased growth in their crystallite sizes, which are calculated to be 68 nm and 94 nm. This was verified by SEM and TEM images (Fig. 2e and f), in which the longitudinally arranged particles of *nc*-Nb_2O_5-800 and *nf*-Nb_2O_5-800 have average diameters of 80 nm and 131 nm, respectively. It is well known that monoclinic Nb_2O_5 typically forms above 1000 °C. However, for our samples, further raising the temperature to 1100 °C only induced particle sintering, resulting in larger particles, while the crystalline phase remained in the orthorhombic structure (ESI, Fig. S6†). Therefore, the heating time was subsequently increased from 2 hours to 10 hours, which successfully yielded highly crystalline monoclinic Nb_2O_5 (Fig. 3d). In stark contrast to the previously discussed *nc*-Nb_2O_5 and *nf*-Nb_2O_5, prismatic crystals were obtained for *nc*-Nb_2O_5-1100 and *nf*-Nb_2O_5-1100 (Fig. 2g and h). *nc*-Nb_2O_5-1100 exhibits rod-like prismatic crystals that have not been reported in the literature for monoclinic Nb_2O_5. However, the prismatic crystals of monoclinic *nf*-Nb_2O_5-1100 are comparatively more compact, no longer inheriting the fibre-like morphology characteristic of CNFs. At high temperature, Nb_2O_5 often undergoes partial melting followed by recrystallisation and the molten Nb_2O_5 solidifies to form the prismatic crystals that we observed in the monoclinic Nb_2O_5 samples. Thus, the more intertwining fibrous network of *nf*-NbO*x*A likely facilitated the solidification of more molten Nb_2O_5 in the vicinity to form larger prismatic crystals. Despite reaching the micron range, both monoclinic *nc*-Nb_2O_5-1100 and *nf*-Nb_2O_5-1100 particles are more structured with a larger intergranular space compared to the monoclinic Nb_2O_5 synthesised without the nanocellulose templates (ESI, Fig. S7†).

The photocatalytic efficiencies of the various Nb_2O_5 samples were assessed by their ability to degrade rhodamine B

when exposed to UV irradiation. The concentrations of rhodamine B were determined using Beer's law, with absorbance readings at 554 nm recorded at 30-minute intervals over a span of 120 minutes (Fig. 4). The results in Fig. 4 show that solutions containing either *nc*-Nb_2O_5 or *nf*-Nb_2O_5 exhibit accelerated degradation rates compared to the control solution without a Nb_2O_5 catalyst and the solution containing bulk pseudohexagonal Nb_2O_5 synthesised at 550 °C (bulk Nb_2O_5-550)

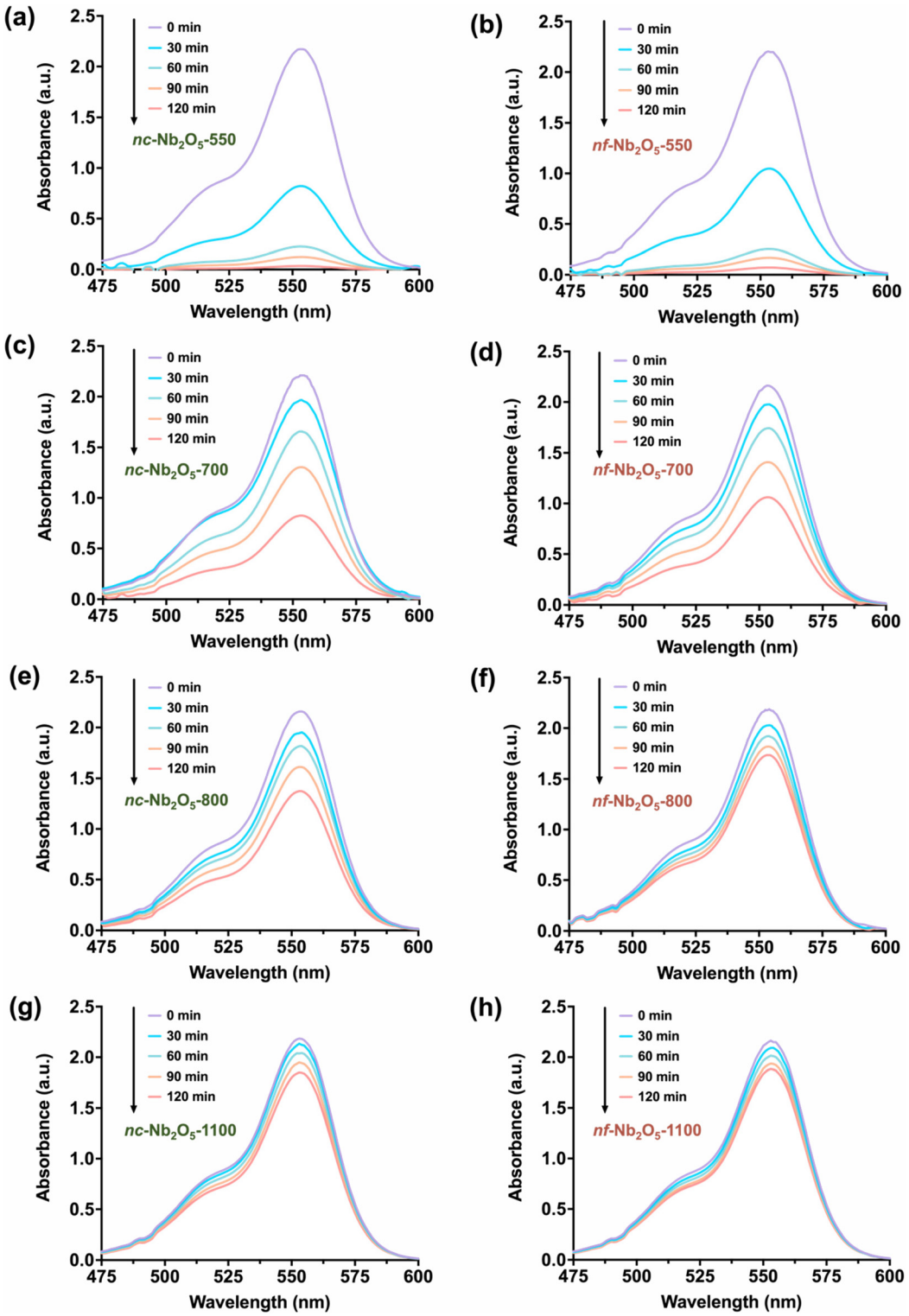

Fig. 4 Absorbance spectral changes of rhodamine B solutions under UV light irradiation in the presence of *nc*-Nb_2O_5 or *nf*-Nb_2O_5 prepared at (a and b) 550 °C, (c and d) 700 °C, (e and f) 800 °C and (g and h) 1100 °C.

(ESI, Fig. S8†). In particular, among the different Nb_2O_5 samples studied, *nc*-Nb_2O_5 presents the highest photocatalytic activity, followed by *nf*-Nb_2O_5, achieving nearly complete rhodamine B degradation within 120 minutes, with degradation percentages of 98% and 96%, respectively. However, degradation percentages declined as the calcination temperatures rose to 700 °C and 800 °C and then to 1100 °C. For *nc*-Nb_2O_5, the degradation percentages decreased from 63% to 37% and further to 13%. Similarly, for *nf*-Nb_2O_5, the degradation percentages decreased from 51% to 21% and then to 16%. The representative decolouration of rhodamine B solutions is shown in Fig. S9,† comparing the colour change of the solutions with and without the *nc*-Nb_2O_5-550 and *nf*-Nb_2O_5-550 photocatalysts. The difference in the photocatalytic efficiencies among the *nc*-Nb_2O_5 and *nf*-Nb_2O_5 samples can be related to the crystal structure of the photocatalyst. Different Nb_2O_5 crystal structures can result in distinctive physicochemical properties.[22,25,39] From Fig. 4 and Fig. S10,† we see that pseudohexagonal Nb_2O_5 (*nc*-Nb_2O_5-550 and *nf*-Nb_2O_5-550) shows the highest rhodamine B degradation, followed by orthorhombic Nb_2O_5 (*nc*-Nb_2O_5-700, *nf*-Nb_2O_5-700, *nc*-Nb_2O_5-800 and *nf*-Nb_2O_5-800) and monoclinic Nb_2O_5 (*nc*-Nb_2O_5-1100 and *nf*-Nb_2O_5-1100). Taken together, these results suggested that as the temperature rises, the crystal structure of Nb_2O_5 becomes more crystalline and organised. We believe that this change distorts the polyhedral structure of Nb_2O_5, decreasing their photocatalytic activity.[25]

Conclusions

We have demonstrated the use of nanocelluloses as sustainable biomaterials to structure Nb_2O_5 polymorphs using polymer-grafted cellulose nanocrystals and cellulose nanofibers. The fabrication of Nb_2O_5 polymorphs was achieved by simple electrostatic complexation between the NbO*x*A precursor and the PDMAEMA shell of the nanocellulose polymer templates. Upon heat treatment, one-dimensional Nb_2O_5 was synthesized, inheriting the interconnected structure of the nanocelluloses. Specifically, by controlling the calcination temperature, we produced phase-pure TT-Nb_2O_5, T-Nb_2O_5 and H-Nb_2O_5, with particle sizes ranging from the nanoscale to the microscale. In addition, we tested the photocatalytic ability of the as-synthesized *nc*-Nb_2O_5 and *nf*-Nb_2O_5 to break down rhodamine B under UV light. Specifically, pseudohexagonal *nc*-Nb_2O_5 and *nf*-Nb_2O_5 show the highest photocatalytic activity among the *nc*-Nb_2O_5 and *nf*-Nb_2O_5 samples tested which we attribute to having more active sites associated with lower crystallinity.

Author contributions

M. M. conceived the idea and supervised the research with C. D. L. Y. T. C and M. M. planned and developed the experimental setup. Y. T. C. performed all the experiments and analysed the data. S. S. A. and N. A. provided the pristine CNC and CNF materials. All the authors discussed the results. Y. T. C. and M. M. co-wrote the manuscript with inputs from all the authors. The authors declare no conflict of interest.

Data availability

The authors declare that the data supporting the findings of this study are available within the paper and its ESI.† Raw data files can be found on the OSF server using this read-only link: **https://osf.io/wstby/?view_only=1ffef41b4daa4ee2b00d218629c8f938**. Should any raw data files be needed in another format, they are available from the corresponding author upon reasonable request.

Conflicts of interest

There are no conflicts to declare.

Acknowledgements

M. M. and C. D. L. acknowledge the Australian Research Council for their Future Fellowship (FT200100185, M. M.) and Discovery Projects (DP230100558, C. D. L.; DP220100452, M. M.), respectively. This research was facilitated by access to Sydney Analytical, a core research facility at the University of Sydney. The authors acknowledge the technical and scientific assistance of Sydney Microscopy & Microanalysis, The University of Sydney node of Microscopy Australia. Y. T. C. is a grateful recipient of a University of Sydney International Scholarship (USydIS). S. S. A. acknowledges the funding support from the University of Queensland (UQ) Research Higher Degree Scholarship. N. A. acknowledges the financial support from Advance Queensland Industry Fellowship (AQIRF128-2020) and support received from industry partner Manildra Harwood Sugar trading as Sunshine Sugar. M. M. is a grateful recipient of a University of Sydney Research Accelerator (SOAR) Prize.

References

1 A. A. Oun, S. Shankar and J. W. Rhim, Multifunctional Nanocellulose/Metal and Metal Oxide Nanoparticle Hybrid Nanomaterials, *Crit. Rev. Food Sci. Nutr.*, 2020, **60**(3), 435–460, DOI: **10.1080/10408398.2018.1536966**.

2 L. H. Nguyen, S. Naficy, R. Chandrawati and F. Dehghani, Nanocellulose for Sensing Applications, *Adv. Mater. Interfaces*, 2019, **6**(18), 30–33, DOI: **10.1002/admi.201900424**.

3 P. Lv, X. Lu, L. Wang and W. Feng, Nanocellulose-Based Functional Materials: From Chiral Photonics to Soft Actuator and Energy Storage, *Adv. Funct. Mater.*, 2021, **31**(45), 2104991, DOI: **10.1002/adfm.202104991**.

4 M. Flejszar and P. Chmielarz, Surface-Initiated Atom Transfer Radical Polymerization for the Preparation of Well-Defined Organic–Inorganic Hybrid Nanomaterials, *Materials*, 2019, **12**(18), 3030, DOI: 10.3390/ma12183030.
5 K. Heise, E. Kontturi, Y. Allahverdiyeva, T. Tammelin, M. B. Linder, Nonappa and O. Ikkala, Nanocellulose: Recent Fundamental Advances and Emerging Biological and Biomimicking Applications, *Adv. Mater.*, 2021, **33**(3), 2004349, DOI: 10.1002/adma.202004349.
6 L. Geurds, J. Lauko, A. E. Rowan and N. Amiralian, Tailored Nanocellulose-Grafted Polymer Brush Applications, *J. Mater. Chem. A*, 2021, 17173–17188, DOI: 10.1039/d1ta03264j.
7 T. H. S. Maia, N. M. Larocca, C. A. G. Beatrice, A. J. de Menezes, G. de Freitas Siqueira, L. A. Pessan, A. Dufresne, M. P. França and A. de Almeida Lucas, Polyethylene Cellulose Nanofibrils Nanocomposites, *Carbohydr. Polym.*, 2017, **173**, 50–56, DOI: 10.1016/j.carbpol.2017.05.089.
8 T. Xu, H. Du, H. Liu, W. Liu, X. Zhang, C. Si, P. Liu and K. Zhang, Advanced Nanocellulose-Based Composites for Flexible Functional Energy Storage Devices, *Adv. Mater.*, 2021, **33**(48), 2101368, DOI: 10.1002/adma.202101368.
9 S. Shafiei-Sabet, W. Y. Hamad and S. G. Hatzikiriakos, Rheology of Nanocrystalline Cellulose Aqueous Suspensions, *Langmuir*, 2012, **28**(49), 17124–17133, DOI: 10.1021/la303380v.
10 P. Amani, N. Amiralian, S. S. A. Athukoralalage and M. Firouzi, Eco-Efficient Pickering Foams: Leveraging Sugarcane Waste-Derived Cellulose Nanofibres, *J. Mater. Chem. A*, 2023, **11**(44), 24379–24389, DOI: 10.1039/d3ta04917e.
11 J. Tang, R. M. Berry and K. C. Tam, Stimuli-Responsive Cellulose Nanocrystals for Surfactant-Free Oil Harvesting, *Biomacromolecules*, 2016, **17**(5), 1748–1756, DOI: 10.1021/acs.biomac.6b00144.
12 P. Amani, N. Amiralian, S. S. A. Athukoralalage and M. Firouzi, Eco-Efficient Pickering Foams: Leveraging Sugarcane Waste-Derived Cellulose Nanofibres, *J. Mater. Chem. A*, 2023, **11**(44), 24379–24389, DOI: 10.1039/D3TA04917E.
13 M. Kaushik and A. Moores, Review: Nanocelluloses as Versatile Supports for Metal Nanoparticles and Their Applications in Catalysis, *m*, 2016, **18**(3), 622–637, DOI: 10.1039/C5GC02500A.
14 M. N. F. Norrrahim, N. M. Nurazzi, M. A. Jenol, M. A. A. Farid, N. Janudin, F. A. Ujang, T. A. T. Yasim-Anuar, S. U. F. Syed Najmuddin and R. A. Ilyas, Emerging Development of Nanocellulose as an Antimicrobial Material: An Overview, *Mater. Adv.*, 2021, **2**(11), 3538–3551, DOI: 10.1039/D1MA00116G.
15 Y. Wu, Y. Liang, C. Mei, L. Cai, A. Nadda, Q. Van Le, Y. Peng, S. S. Lam, C. Sonne and C. Xia, Advanced Nanocellulose-Based Gas Barrier Materials: Present Status and Prospects, *Chemosphere*, 2022, **286**(P3), 131891, DOI: 10.1016/j.chemosphere.2021.131891.
16 A. Morsy, A. S. Mahmoud, A. Soliman, H. Ibrahim and E. Fadl, Improved Anti-Biofouling Resistances Using Novel Nanocelluloses/Cellulose Acetate Extracted from Rice Straw Based Membranes for Water Desalination, *Sci. Rep.*, 2022, **12**(1), 4386, DOI: 10.1038/s41598-022-08324-8.
17 Y. T. Cheng, Q. Xia, H. Liu, M. B. Solomon, C. D. Ling and M. Müllner, Polymer Brush-Grafted Cellulose Nanocrystals for the Synthesis of Porous Carbon-Coated Titania Nanocomposites, *Polym. Chem.*, 2023, **14**(18), 2181–2189, DOI: 10.1039/D3PY00194F.
18 M. Morits, V. Hynninen, N. Nonappa, A. Niederberger, O. Ikkala, A. H. Gröschel and M. Müllner, Polymer Brush Guided Templating on Well-Defined Rod-like Cellulose Nanocrystals, *Polym. Chem.*, 2018, **9**(13), 1650–1657, DOI: 10.1039/C7PY01814B.
19 S. Wohlhauser, G. Delepierre, M. Labet, G. Morandi, W. Thielemans, C. Weder and J. O. Zoppe, Grafting Polymers from Cellulose Nanocrystals: Synthesis, Properties, and Applications, *Macromolecules*, 2018, **51**(16), 6157–6189, DOI: 10.1021/acs.macromol.8b00733.
20 R. Wu, S. Shen, G. Xia, F. Zhu, C. Lastoskie and J. Zhang, Soft-Templated Self-Assembly of Mesoporous Anatase TiO2/Carbon Composite Nanospheres for High-Performance Lithium Ion Batteries, *ACS Appl. Mater. Interfaces*, 2016, **8**(31), 19968–19978, DOI: 10.1021/acsami.6b03733.
21 Y. T. Cheng, Q. Xia, H. Liu, M. B. Solomon, E. R. L. Brisson, L. D. Blackman, C. D. Ling and M. Müllner, Tunable Polymer Nanoreactors from RAFT Polymerization-Induced Self-Assembly: Fabrication of Nanostructured Carbon-Coated Anatase as Battery Anode Materials with Variable Morphology and Porosity, *ACS Appl. Mater. Interfaces*, 2023, **15**(9), 12261–12272, DOI: 10.1021/acsami.2c18928.
22 K. Su, H. Liu, Z. Gao, P. Fornasiero and F. Wang, Nb2O5-Based Photocatalysts, in *Advanced Science*, John Wiley and Sons Inc., 2021. DOI: 10.1002/advs.202003156.
23 H. Liu, N. Gao, M. Liao and X. Fang, Hexagonal-like Nb2O5 Nanoplates-Based Photodetectors and Photocatalyst with High Performances, *Sci. Rep.*, 2015, **5**, 7716, DOI: 10.1038/srep07716.
24 C. Shi, K. Xiang, Y. Zhu, W. Zhou, X. Chen and H. Chen, Box-Implanted Nb2O5 Nanorods as Superior Anode Materials in Lithium Ion Batteries, *Ceram. Int.*, 2017, **43**(15), 12388–12395, DOI: 10.1016/j.ceramint.2017.06.105.
25 C. L. Ücker, F. C. Riemke, N. F. de Andrade Neto, A. d. A. G. Santiago, T. J. Siebeneichler, N. L. V. Carreño, M. L. Moreira, C. W. Raubach and S. Cava, Influence of Nb2O5 Crystal Structure on Photocatalytic Efficiency, *Chem. Phys. Lett.*, 2021, **764**, 138271, DOI: 10.1016/j.cplett.2020.138271.
26 L. Guo, X. Yao, Z. Wang, C. Luo, L. Zhou, F. Liu, R. Zhang and X. Wang, Hierarchically Periodic Macroporous Niobium Oxide Architecture for Enhanced Hydrogen Evolution, *Small*, 2024, **20**(25), 2310753, DOI: 10.1002/smll.202310753.

27 H. Park, D. Lee and T. Song, High Capacity Monoclinic Nb2O5 and Semiconducting NbO2 Composite as High-Power Anode Material for Li-Ion Batteries, *J. Power Sources*, 2019, **414**, 377–382, DOI: 10.1016/j.jpowsour.2019.01.015.

28 X. Liu, G. Liu, H. Chen, J. Ma and R. Zhang, Facile Synthesis of Nb2O5 Nanobelts Assembled from Nanorods and Their Applications in Lithium Ion Batteries, *J. Phys. Chem. Solids*, 2017, **111**, 8–11, DOI: 10.1016/j.jpcs.2017.07.007.

29 L. Wang, X. Bi and S. Yang, Partially Single-Crystalline Mesoporous Nb 2 O 5 Nanosheets in between Graphene for Ultrafast Sodium Storage, *Adv. Mater.*, 2016, **28**(35), 7672–7679, DOI: 10.1002/adma.201601723.

30 M. Liu, C. Yan and Y. Zhang, Fabrication of Nb2O5 Nanosheets for High-Rate Lithium Ion Storage Applications, *Sci. Rep.*, 2015, **5**, 8326, DOI: 10.1038/srep08326.

31 A. L. Viet, M. V. Reddy, R. Jose, B. V. R. Chowdari and S. Ramakrishna, Nanostructured Nb 2 O 5 Polymorphs by Electrospinning for Rechargeable Lithium Batteries, *J. Phys. Chem. C*, 2010, **114**(1), 664–671, DOI: 10.1021/jp9088589.

32 M. Müllner, J. Cui, K. F. Noi, S. T. Gunawan and F. Caruso, Surface-Initiated Polymerization within Mesoporous Silica Spheres for the Modular Design of Charge-Neutral Polymer Particles, *Langmuir*, 2014, **30**(21), 6286–6293, DOI: 10.1021/la501324r.

33 R. F. Albers, W. Yan, M. Romio, E. R. Leite, N. D. Spencer, K. Matyjaszewski and E. M. Benetti, Mechanism and Application of Surface-Initiated ATRP in the Presence of a Zn 0 Plate, *Polym. Chem.*, 2020, **11**(44), 7009–7014, DOI: 10.1039/D0PY01233E.

34 Z. Zhang, G. Sèbe, Y. Hou, J. Wang, J. Huang and G. Zhou, Grafting Polymers from Cellulose Nanocrystals via Surface–initiated Atom Transfer Radical Polymerization, *J. Appl. Polym. Sci.*, 2021, **138**(48), 51458, DOI: 10.1002/app.51458.

35 M. Morits, J. R. McKee, J. Majoinen, J. M. Malho, N. Houbenov, J. Seitsonen, J. Laine, A. H. Gröschel and O. Ikkala, Polymer Brushes on Cellulose Nanofibers: Modification, SI-ATRP, and Unexpected Degradation Processes, *ACS Sustainable Chem. Eng.*, 2017, **5**(9), 7642–7650, DOI: 10.1021/acssuschemeng.7b00972.

36 Z. Zhang, K. C. Tam, G. Sèbe and X. Wang, Convenient Characterization of Polymers Grafted on Cellulose Nanocrystals via SI-ATRP Without Chain Cleavage, *Carbohydr. Polym.*, 2018, **199**, 603–609, DOI: 10.1016/j.carbpol.2018.07.060.

37 K. M. Eblagon, A. Malaika, K. Ptaszynska, M. F. R. Pereira and J. L. Figueiredo, Impact of Thermal Treatment of Nb2O5 on Its Performance in Glucose Dehydration to 5-Hydroxymethylfurfural in Water, *Nanomaterials*, 2020, **10**(9), 1685, DOI: 10.3390/nano10091685.

38 U. Holzwarth and N. Gibson, The Scherrer Equation versus the "Debye-Scherrer Equation", in *Nature Nanotechnology*, Nature Publishing Group, 2011, p. 534. DOI: 10.1038/nnano.2011.145.

39 C. L. Ücker, L. T. Gularte, C. D. Fernandes, V. Goetzke, E. C. Moreira, C. W. Raubach, M. L. Moreira and S. S. Cava, Investigation of the Properties of Niobium Pentoxide for Use in Dye-Sensitized Solar Cells, *J. Am. Ceram. Soc.*, 2019, **102**(4), 1884–1892, DOI: 10.1111/jace.16080.